

A Search for Non-triggered Gamma Ray Bursts in the BATSE Data Base

Jefferson M. Kommers,¹ Walter H. G. Lewin,¹ Chryssa Kouveliotou,^{2,3} Jan van Paradijs,^{4,5}
Geoffrey N. Pendleton,⁴ Charles A. Meegan,³ and Gerald J. Fishman³

ABSTRACT

We describe a search of archival data from the Burst and Transient Source Experiment (BATSE). The purpose of the search is to find astronomically interesting transients that did *not* activate the burst detection (or “trigger”) system onboard the spacecraft. Our search is sensitive to events with peak fluxes (on the 1.024 s time scale) that are lower by a factor of ~ 2 than can be detected with the onboard burst trigger. In a search of 345 days of archival data, we detected 91 events in the 50–300 keV range that resemble classical gamma ray bursts but that did not activate the onboard burst trigger. We also detected 110 low-energy (25–50 keV) events of unknown origin which may include activity from SGR 1806–20 and bursts and flares from X-ray binaries. This paper gives the occurrence times, estimated source directions, durations, peak fluxes, and fluences for the 91 gamma ray burst candidates. The direction and intensity distributions of these bursts imply that the biases inherent in the onboard trigger mechanism have not significantly affected the completeness of the published BATSE gamma ray burst catalogs.

Subject headings: gamma rays: bursts

¹Department of Physics and Center for Space Research, Massachusetts Institute of Technology, Cambridge, MA 02139

²Universities Space Research Association, Huntsville, AL 35800

³NASA/Marshall Space Flight Center, Huntsville, AL 35812

⁴University of Alabama in Huntsville, Huntsville, AL 35812

⁵University of Amsterdam, Amsterdam, Netherlands

1. Introduction

Since 1991 April 19 the Burst and Transient Source Experiment (BATSE) on the *Compton Gamma Ray Observatory* (CGRO) has been detecting gamma ray bursts (GRBs) and other high-energy transients with unprecedented sensitivity (Fishman et al. 1989; Fishman et al. 1994b; Meegan et al. 1996). The 1122 GRBs in the 3B catalog show an isotropic angular distribution and a spatially inhomogeneous intensity distribution (Meegan et al. 1992; Meegan et al. 1996). Despite extensive analysis, however, the origin of GRBs remains unknown; see recent reviews by Fishman & Meegan (1995), Briggs (1995), and Hartmann (1995).

The detection of GRBs and other high-energy transients with BATSE is controlled by a real-time burst detection algorithm running onboard the spacecraft (Fishman et al. 1989). The onboard computer continuously monitors the count rates in each of the eight Large Area Detectors (LADs). When the count rates exceed a certain threshold, the computer signals a “burst trigger” and data are collected at high temporal and spectral resolution for a limited time interval. Even in the absence of a burst trigger, however, data are recorded at lower resolution in the continuous data types. For most of the mission, the criteria for a burst trigger have been that the 50–300 keV count rates in two detectors simultaneously increase by more than 5.5 times the expected root-mean-square background fluctuations on any of three time scales: 64 ms, 256 ms, or 1024 ms. The average background rate for each detector is recomputed every 17.408 s (Fishman et al. 1989).

By definition all of the GRBs listed in the 1B, 2B, and 3B catalogs satisfy the requirements for a burst trigger (Fishman et al. 1994b; Meegan et al. 1996). Other transient phenomena that are unrelated to GRBs can also lead to a burst trigger. Examples include solar flares, terrestrial magnetospheric disturbances, bursts and flares from X-ray binaries, and activity from soft gamma ray repeaters (SGRs). Such events are classified appropriately by the BATSE team.

A GRB or other transient phenomenon may have characteristics such that it does *not* lead to a burst trigger onboard the spacecraft but it nevertheless leaves a statistically significant signal in the continuous data. For example, a GRB or other transient may be too faint to achieve the necessary statistical signif-

icance for a trigger; it may have a time profile that biases the onboard background average; or it may have too few counts in the 50–300 keV range.

A burst can also occur while the onboard trigger is disabled for technical reasons. Following a burst trigger, the high resolution data collected during the burst accumulation interval are gradually telemetered to the ground during the following 90 minutes. During this read out period the onboard burst trigger is disabled on the 256 ms and 1024 ms time scales, and the 64 ms threshold is set to the maximum rate of the burst being read out. The onboard burst trigger is also disabled when the spacecraft passes through regions with a high probability of triggering on atmospheric particle precipitation events (Fishman et al. 1994b).

In this paper, we describe a retrospective search of the archival continuous data from BATSE for statistically significant GRBs and other transients that did *not* cause a burst trigger onboard the spacecraft. A search for these “non-triggered” (or “untriggered”) events in the 50–300 keV range is expected to find GRBs that are generally fainter than those cataloged previously. A concurrent search for non-triggered events in the lowest discriminator channel (25–50 keV) is expected to find activity from other astronomical sources, including bursts and flares from X-ray binaries and activity from SGRs. This ongoing project is an extension of previous work by Rubin et al. (1993), Van Paradijs et al. (1993), and Kommers et al. (1996). Other retrospective searches for GRBs in the BATSE data (using techniques different from those described here) have been discussed by Skelton & Mahoney (1994) and by Young et al. (1996).

2. Search Algorithm

A retrospective search of archival data can take advantage of burst detection algorithms that would have been impractical to implement onboard the spacecraft. The choice of a detection scheme to look for non-triggered events therefore involves trade-offs between the detection efficiency of the method for a given class of events and the resources (both computational and human) needed to implement it. In this section we describe a search algorithm which is loosely based on the one used onboard the spacecraft but which has proved more sensitive. The next section will discuss its efficiency for detecting transients with certain characteristics.

We will refer to all events detected by our off-line search of archival data as “laboratory triggers.” The events previously detected by the onboard burst trigger mechanism will be called “onboard triggers.” Some onboard triggers will be flagged by our off-line search and so they will also be laboratory triggers. Events that were detected *only* by our off-line search will be called “non-triggered events.”

For most of the mission the onboard trigger criterion has required that the count rate in two detectors simultaneously increase by at least $5.5\sigma_B$ above the nominal background level, where σ_B is the standard deviation of the expected background counts due to counting statistics. As a result, the BATSE detectors provide anisotropic sky exposure over short time periods (Fishman et al. 1989; Fishman et al. 1994b). The cosine-like change in the detectors’ effective area with source viewing direction causes the onboard trigger to be less sensitive to faint bursts with directions directly in front of one of the detectors than to ones with directions mid-way between two detector normals (Brock et al. 1991). For example, a $10\sigma_B$ event occurring directly in front of a detector may produce only a $3.5\sigma_B$ signal in the second most brightly illuminated detector and it would thus fail to trigger onboard. On the other hand, the same event incident along a direction mid-way between two detector normals would register approximately $7.1\sigma_B$ in both detectors and would comfortably cause an onboard trigger.

The onboard trigger mechanism relies on a background rate that is computed during a 17.408 s time interval occurring before the time bin being tested. A rising or falling background can therefore bias the background estimate to be too low or too high, respectively. A slowly rising transient may itself bias the background estimate upwards to such an extent that it fails to cause an onboard burst trigger, even though it is otherwise intense enough to be above the minimum detection threshold.

Our retrospective search procedure partially combats the directional detection anisotropy and the rising/falling background bias. We form a time series to be searched by combining the relevant energy channels from the DISCLA data. This data type provides the count rates in each detector integrated over 1024 ms time bins. Four discriminator energy channels (numbered 1 through 4) are available: 25–50 keV, 50–100 keV, 100–300 keV, and > 300 keV. When searching for GRBs, the sum of channels 2 and 3

(50–300 keV) gives optimal sensitivity. When searching for low-energy transients such as bursts and flares from X-ray binaries or SGRs the lowest energy channel (channel 1, 25–50 keV) is most sensitive. A sum of channels 1, 2, and 3 provides a further “catch-all” search. After summing the appropriate energy channels, the time series are rebinned in time (if necessary) to search on time scales longer than the 1024 ms DISCLA sampling period. The resulting time series are then searched sequentially to see if any data meet our laboratory trigger criteria.

To signal a laboratory trigger, we first determine from the time series being searched a nominal background level for each detector. To estimate $B_d(k)$, the number of background counts expected in detector d for the time bin k , we use a linear fit to the data in time bins $k - N_b, \dots, k - 1$ and $k + 1 + N_b, \dots, k + 2N_b$. Here the number of background bins, N_b , is specified for each time scale. Unlike the onboard trigger, the off-line search uses data before and after the time bin being tested.¹ This method reduces the bias (discussed above) caused by slowly rising or falling background levels.

Temporally contiguous data are not always available because of telemetry gaps and spacecraft passages through regions of high particle flux, such as the South Atlantic Anomaly (SAA). In such cases the background estimate discussed here cannot be formed. We only test bins for which we can estimate the background with the above procedure, so our search is not sensitive to bursts that occur during the N_b bins after, or the $2N_b$ bins before, a data gap.

Let $C_d(k)$ be the measured number of counts in time bin k for detector d . We define the “significance” of that detector to be $S_d(k) = [C_d(k) - B_d(k)]/\sqrt{B_d(k)}$. Our laboratory trigger criteria are that the two greatest values of the 8 significances $S_d(k)$, call them s_1 and s_2 , must be such that $s_1 \geq s_2 \geq M$ and $s_1 + s_2 \geq \Sigma$. These criteria ensure that at least two detectors simultaneously experience a statistically significant upward fluctuation, but they are also more sensitive to events incident along detector normals than the onboard criteria.

¹The bin, k , being tested is not centered in the gap of N_b bins which separates the fitted intervals. This somewhat arbitrary choice evolved out of various triggering schemes which were tried, including one where the background was always estimated based on the N_b bins immediately prior to the one being tested. The scheme chosen performed well on 14 days of data that were used to test various laboratory trigger criteria.

The values chosen for M , Σ , and N_b for the searches reported here are shown in Table 1. They were chosen to keep the actual number of detections per day of data searched (due to the activity of real sources) at a manageable level of about 20 per day.

A more sensitive search could be conducted using other laboratory trigger criteria. For example, the effective detector area achieved by adding the rates in each set of 3 contiguous detectors would produce time series with higher signal-to-noise ratios for activity from real sources. The caveat to a more sensitive search is the corresponding increase in the rate of “false triggers” due to solar activity, variability from X-ray binaries, particle precipitation events, Earth occultation steps, and phosphorescence spikes (which occur when high-energy particles interact in the detectors). During outbursts of bright X-ray binaries, our laboratory trigger has detected hundreds of events per day due to variability from Vela X-1, A0535+26, and GRO J0422+32.

For our laboratory trigger criteria, the number of detections expected from statistical fluctuations alone can be estimated by considering the “phase space” defined by s_1 and s_2 . The number of counts in each time bin of the DISCLA data type is large enough that the Poisson statistics can be treated in the Gaussian approximation, so that the $S_d(k)$ are independent and normally distributed with zero mean and unit variance. The laboratory trigger criteria define a region A in the (s_1, s_2) plane in which measured values s_1^* and s_2^* will be flagged by our search. This area is sketched in Figure 1.

The probability P_{stat} that a randomly selected set of 8 significances S_d will meet or exceed the laboratory trigger criteria is estimated by first integrating the bivariate normal distribution (centered on the origin) over the allowed area A in the (s_1, s_2) plane. Next, we multiply by 8 ways to select the most significant detector (s_1) and the remaining 7 ways to select the second most significant (s_2). The final expression is

$$P_{stat} = \left[\iint_A \frac{1}{2\pi} \exp\left(-\frac{s_1^2 + s_2^2}{2}\right) ds_1 ds_2 \right] \times 7 \times 8. \quad (1)$$

If there are N time bins searched per day, the number of detections expected from purely statistical fluctuations is $P_{stat} \times N$ per day. This quantity is shown in the last column of Table 1 for a representative value of $N = 5.0 \times 10^4$. Although the searches are not statistically independent, we would expect no more

than 8 detections due solely to statistical fluctuations in a search of 100 days of data. Furthermore only a fraction of these will have properties consistent with astronomical source activity.

In practice we find many more laboratory triggers than can be expected from purely statistical fluctuations. This is because the time series we are searching are not Poissonian. They are dominated by the activity of real sources. Astronomical objects, the sun, terrestrial photon sources, and the interaction of particles in the detectors contribute to the count rates. Figure 2 shows an integral distribution of $S_d(k)$ for a single detector ($d = 0$) taken from a search of one day of data on the 1.024 s time scale. For comparison, the expectation from a normal distribution with zero mean and unit variance is also shown. The excess over what is expected from a normal distribution reflects both deficiencies in the background estimation and the activity of real sources, although no laboratory triggers were detected by our off-line search in this detector on the day shown.

3. Sensitivity

The search strategy described above is expected to detect bursts that were fainter than those detected by the onboard trigger mechanism. In this section, we estimate the efficiency of the search algorithm for detecting events with certain physical characteristics. In general the ability of our search strategy to detect an event depends on its peak flux (as measured on the search time scale), its time profile, the background levels in the detectors, and the spacecraft orientation with respect to the source direction. Here we will estimate the trigger efficiency and sky exposure of our off-line search strategy assuming an event profile for which a single time bin completely determines our ability to detect the event. The effects of a more complicated time profile are then considered separately for a simplified case of “slow-rising” events that would have biased the onboard background estimate.

3.1. Trigger Efficiency

We define the trigger efficiency $E(P, \nu, \alpha, \delta, t)$ to be the probability that an event with given physical characteristics will satisfy the laboratory trigger criteria. The event is modeled in terms of its peak flux on the time scale of the search (P), power-law photon spectral index (ν), source direction in equatorial

coordinates (α, δ) , and time of occurrence during the mission (t). The background rates in the detectors, the spacecraft orientation, and the geographic position of the spacecraft must also be known to estimate E , but these quantities are known from the data once t is specified. The time profile of the event is considered to be a square pulse that occupies a single time bin.

For a particular spacecraft orientation and position, the mean count rates expected from an event with given values of P , ν , α , and δ can be computed by adding the “direct” count rates found from the BATSE instrument response matrix to the “scattered” count rates expected from the scattering of incident photons by the Earth’s atmosphere. The instrument response matrices and atmospheric scattering model are described further in Pendleton et al. (1995) and Meegan et al. (1996).² The resulting total count rates are multiplied by the time binning interval to obtain the expected counts (above background) in a single bin of the time series for each detector; we denote these quantities by C_d^* . The expected background counts, B_d , are estimated from the measured rates at time t and the expected significances in the detectors are calculated as $S_d^* = C_d^*/\sqrt{B_d}$. Let s_1^* and s_2^* be the the greatest and second greatest of the S_d^* , respectively.

The trigger efficiency, E , is the probability that a measurement of a pair (s_1, s_2) will meet the laboratory trigger criteria. The counting statistics imply that our measurement, (s_1, s_2) , is drawn from a bivariate normal distribution with unit variances centered on the expected significances, (s_1^*, s_2^*) . The probability that we detect the given event is therefore estimated by integrating this distribution over the area, A (shown in Figure 1), in which the trigger criteria are satisfied:

$$E = \iint_A \frac{1}{2\pi} \exp\left[-\frac{(s_1 - s_1^*)^2}{2}\right] \exp\left[-\frac{(s_2 - s_2^*)^2}{2}\right] ds_1 ds_2. \quad (2)$$

We evaluate E on a three-dimensional grid composed of 9 peak fluxes, 252 source directions, and 4992 times per orbital precession period of *CGRO* (i.e., every 15 minutes). The photon spectral index is fixed at

$\nu = 2.0$. The 9 peak fluxes were chosen to span an intensity range where the efficiency varies significantly. The 252 source directions are nearly isotropically distributed on the unit sphere (Tegmark 1996). The 4992 times per orbital precession period were chosen to thoroughly sample the range of background variations. For points where the source direction is behind the Earth or no searchable data are available, E is set to zero. This calculation must be repeated for each time scale and energy channel combination in our search.

Figure 3 shows E as a function of P for events searched on the 1024 ms and 4096 ms time scales in the 50–300 keV range. The source directions and times of occurrence have been averaged. For comparison, the trigger efficiency on the 1024 ms time scale from the BATSE 1B catalog is also shown (Fishman et al. 1994b).

For the 1024 ms time scale, Figure 3 shows that our search is nearly complete near the BATSE threshold (~ 0.2 ph cm⁻² s⁻¹). Our off-line search should detect about 50% of events with peak fluxes lower by a factor of ~ 2 than the onboard 50% completeness limit. For events that maintain their peak flux for at least 4 s or 8 s, the searches on the 4096 ms and 8192 ms time scales can reach even lower peak fluxes. The values of $E(P)$ shown in Figure 3 vary by only a few percent between spacecraft orbital precession periods (52 days for *CGRO*).

The sky coverage of our search is determined by the angular distribution of $E(P, \nu, \alpha, \delta)$, where P and ν are fixed and t has been averaged. If T is the total time period covered by the data searched, then $T \times E(P, \nu, \alpha, \delta)$ gives the total amount of time that our search was sensitive to an event with the given intensity, spectral index, and source direction. In practice our search covers many orbits, so the dependence on the equatorial right ascension (α) averages out. Figure 4 shows the sky exposure as a function of declination (δ) for events with $P \geq 0.5$ ph s⁻¹ cm⁻² on the 1024 ms time scale and $\nu = 2.0$. The decreased exposure near the celestial equator is due to Earth blockage. The Southern Hemisphere gets less exposure than the Northern Hemisphere due to passages through the SAA.

3.2. Sensitivity to “slow-risers”

The chances that our search detects a given event also depend on its time profile in our time series. For

²The detector response and atmospheric scattering matrices used in this work were provided by the BATSE team. We also made use of some elements of the BACODINE burst location code (Scott Barthelmy, private communication) which is based on an early version of the BATSE LOCBURST code.

example, an event with a peak flux near the detection threshold that is shaped like a square pulse occupying N time bins will have N statistical chances to meet or exceed the trigger criteria. In such a case the trigger efficiency calculated above will be an underestimate.

On the other hand, the event profile may be such that it biases the nominal background rate used by the search algorithm and artificially raises the detection threshold. Then the trigger efficiency calculated above is an overestimate. This case is more serious as it implies that the search could miss a population of such events even though their peak flux is well above the nominal minimum detection threshold. Both the onboard trigger mechanism and our off-line search are subject to this limitation.

The most problematic time profile is one which both rises and decays slowly on a time scale long compared to the background averaging with no significant rapid variability. This case is difficult to distinguish from background variations arising from the spacecraft environment. Neither our search nor the onboard trigger has appreciable sensitivity to events of this type. They are even unlikely to be evident in a close visual inspection of the count rates.

An event that rises slowly and then either falls off quickly or subsequently goes into a more complicated profile can usually be identified as a transient, however. We will call such an event a “slow-riser.” The onboard trigger mechanism has particular trouble with slow-risers because it can only base its background estimate on count rates measured over some 17.408 s interval that occurred some time during the 34.8 s before the time bin being tested. Lingenfelter & Higdon (1996) have discussed this effect for the onboard burst trigger. Here we estimate the extent to which our off-line search algorithm is sensitive to slow-risers.

The profile of an idealized slow-riser is shown in Figure 5. The event is characterized by a peak amplitude, s , measured in sigmas above background, and a slope, r , measured in sigmas per second, where one sigma is one standard deviation of the expected background fluctuations. The total duration of the event is s/r . To estimate our sensitivity to such events, we generated a grid of peak amplitudes and a grid of slopes. For each peak amplitude and slope, we generated 5000 events with a background level of 1000 counts s^{-1} and Poisson noise to mimic the counting statistics. We then used our detection algorithm to find the fraction of events that met our off-line trig-

ger threshold and the fraction of events that met the onboard trigger threshold.

The results are shown in Figure 6, which shows contours of detection probability for (idealized) events with maximum significance, s , and slope, r , when searching on the 1024 ms time scale. Evidently our laboratory detection algorithm is more sensitive to slow-risers than the onboard trigger mechanism. This is due both to the lower detection threshold and to the use of data before and after the time bin being tested when forming the background estimate. Slow-risers with no subsequent variability that are both longer than about 30 s and fainter than 5σ (about 0.3–0.5 photons $cm^{-2} s^{-1}$ in the 50–300 keV range) are unlikely to be found by our 1024 ms off-line search. The 4096 ms and 8192 ms searches are sensitive to longer events, however.

The idealized profile used for these estimates may not be representative of the faintest or longest transients since the typical profiles of those events are not known a priori. The simple case presented here shows that our search algorithm is more sensitive to *some* slow-rising bursts.

4. Classification and Analysis of Events

We visually inspect each laboratory trigger flagged by our off-line search to separate the events into useful categories.

We first examine plots of the count rates in each of the eight detectors at the time of the laboratory trigger. This information is adequate to exclude from further analysis the majority of features in the data that are not interesting in the context of our search. Common examples of such features are occultation steps, phosphorescence spikes, and magnetospheric particle precipitation events.

Occultation steps due to bright sources (such as Cyg X-1) rising above (or setting below) the Earth’s limb typically appear as sustained increases (or decreases) in the count rates in two or more detectors. This signature is not generally consistent with the burst-like transients we seek.

Phosphorescence spikes due to the interaction of high-energy particles in the detectors typically appear in the DISCLA data as short (< 1.024 s), intense (> 1000 counts s^{-1}) spikes in the lowest energy channel (25–50 keV) of a single detector. The intense signal in one detector with no coincident signal in a second detector is inconsistent with a point source of pho-

tons.

Magnetospheric particle precipitation events occur when particles (mostly electrons with energies of tens of eV to tens of MeV) that are usually trapped in the radiation belts by the Earth’s magnetosphere are released into the upper atmosphere (Burgess & Inan 1993). The LADs detect the bremsstrahlung generated as precipitating particles interact in the atmosphere or in the spacecraft (Horack et al. 1992 and references therein). These events can appear in the data in three different ways as discussed by Horack et al. (1992). Events of the first kind show a smooth rise and decay with comparable intensities in all eight detectors; this signature is inconsistent with a point source of photons. The second kind of event arises when the precipitation occurs at some distance from the spacecraft, so that it appears only in the detectors on one side of the satellite. Because the source of radiation is relatively nearby, however, the orbital motion of *CGRO* gives the event different profiles in different detectors. The third kind of event shows rapid variability with complex temporal structure, and can closely mimic a GRB. Such events can be recognized if they show characteristics from the first two classes, such as appearance in opposite-facing detectors or inconsistent time profiles between detectors. These events also exhibit a bremsstrahlung cutoff in their energy spectrum.

If an event does not appear to be any of the above, we define background intervals by hand and estimate the source direction using our version of the BATSE LOCBURST software (see below). We also examine the profile of the event in the 4 DISCLA energy channels.

Events with directions estimated to be behind the Earth are classified as “Earth” events. We have not yet done a detailed analysis of this category, but it is likely to include electron precipitation events occurring below the spacecraft, events from other categories for which we obtained poor direction estimates, and possibly terrestrial gamma ray flashes (TGRFs; Fishman et al. 1994a).

Solar flares are identified based primarily on spectral softness and location. Typical solar flares have most of their counts in DISCLA channel 1, with fewer in channel 2, and fewer still in channel 3. In contrast, typical GRBs have most of their counts in channels 2 and 3, with proportionally less signal in channel 1. Some spectrally hard solar flares are observed, however, so events with directions consistent with the sun

(within uncertainties) are classified as solar. For the search described here we did not compare laboratory trigger times with records of solar activity to separate hard solar flares from GRBs.

Events which appear to be neither terrestrial nor solar and which have sufficient spectral hardness to be seen both in channels 2 and 3 are classified as GRB candidates.

Events which do not make it into any of the previous categories are classified as “unknown”, a category which includes all the low-energy (channel 1 only) events that are not obviously of terrestrial or solar origin. Events with significant counts in channels 1 and 2 (25–100 keV) but not in channel 3 (100–300 keV) are also included in this category.

The classification of laboratory triggers is subjective in cases where there is not an obvious indication of the nature of the event. To compare our classification methods with those of the BATSE team, we can use the 317 onboard triggers that were also laboratory triggers in our search of 345 days of data (see section 5; the remaining 256 triggers were not detected because of gaps in the DISCLA data files). Table 2 shows how these onboard triggers were classified by the BATSE team and by us.

Out of the 221 events that were identified as GRBs by the BATSE team, we classified 198 as GRBs, 10 as solar flares, 4 as magnetospheric events, and 9 in other categories (such as “unknown” or “Earth”). The 10 events that were classified as GRBs by the BATSE team but as solar flares by us all had estimated directions consistent with the sun. We classified them as solar flares because we could not argue that they were GRBs rather than hard solar flares. The 4 BATSE GRBs that we classified as magnetospheric events occurred while the spacecraft was in the vicinity of the SAA or at a maximum (or minimum) geographic latitude, where particle precipitation events are common. The remaining 9 BATSE GRBs that we put in other categories include very short (duration < 1 s) bursts that were difficult to classify due to low signal-to-noise, events for which we estimated the directions to be behind the Earth, and bursts for which there was an unusually low count rate in channel 3 (100–300 keV).

The results in Table 2 show that our classifications agree with those of the BATSE team in most cases. When there is uncertainty between a GRB and a non-GRB origin, our classification is “conservative”

in that we tend towards the non-GRB classification. There were only 2 events out of 200 that we classified as GRBs but that the BATSE team classified as magnetospheric particle precipitation events. Over the course of a year, our tendency to classify hard events occurring near the sun as solar flares introduces a bias against GRBs that occur in the plane of the ecliptic.

For each of the solar flares, GRB candidates, and unknown events we estimate a source direction, intensity, and power-law spectral index using a modified version of the BATSE LOCBURST code. This software uses the BATSE detector response matrices along with a model for the scattering of incident photons by the Earth’s atmosphere to find the count rates expected from an event with intensity P (in photons $\text{cm}^{-2} \text{s}^{-1}$ above 10 keV), power-law spectral index ν , and source direction (θ, ϕ) in *CGRO* coordinates (Fishman et al. 1994b; Pendleton et al. 1995). Let $C_d^i(P, \nu, \theta, \phi)$ denote the model count rates expected in energy channel i of detector d , and let \tilde{C}_d^i denote the measured (background subtracted) count rates with associated statistical measurement uncertainties $\tilde{\sigma}_{i,d}$. To estimate \tilde{P} , $\tilde{\nu}$, $\tilde{\theta}$, and $\tilde{\phi}$ for a given event, the software minimizes the following measure of goodness-of-fit,

$$\chi^2(\tilde{P}, \tilde{\nu}, \tilde{\theta}, \tilde{\phi}) = \sum_{i,d} \left[\frac{\tilde{C}_d^i - C_d^i(\tilde{P}, \tilde{\nu}, \tilde{\theta}, \tilde{\phi})}{\tilde{\sigma}_{i,d}} \right]^2. \quad (3)$$

The measured count rates used for this procedure are mean count rates obtained from the main (most intense) portion of the burst as selected by hand during our visual inspection of the laboratory triggers.

The angular response of the BATSE detectors can allow for multiple, widely separated local minima in the χ^2 parameter space, especially for weak bursts. For example, if a burst has most of its counts in just two detectors it can be equally consistent with two burst directions depending on the choice of the third most brightly illuminated detector. For weak bursts, the statistics may not be good enough to reliably distinguish the third detector. Background variations (due to real source activity) in some detectors can also make it difficult to distinguish the third detector. In such situations, χ^2 can be a strongly non-linear function of the observed rates. The errors on the estimated burst parameters cannot then be reliably estimated from the formal covariance matrix of the fit.

To estimate errors on the model parameters for

each burst, we produce 50 sets of “synthetic” burst rates obtained by drawing from a random distribution with the same means and variances as the measured rates. These 50 sets of synthetic count rates are then subjected to the same χ^2 minimization procedure as the real rates. The variances in the parameters obtained from the synthetic count rates are used to estimate the uncertainty on the parameters $(\tilde{P}, \tilde{\nu}, \tilde{\theta}, \tilde{\phi})$ obtained from the measured count rates.

Using the estimated mean intensity \tilde{P} we obtain a conversion factor from counts s^{-1} in the most brightly illuminated detector to units of $\text{ph cm}^{-2} \text{s}^{-1}$ in the 50–300 keV range. The peak flux and fluence of each event in physical units are then determined by multiplying the corresponding measured counts by this conversion factor. The durations of events are characterized by the T_{50} and T_{90} duration measures, which are the time intervals during which the burst fluence increases from 25% to 75% and from 5% to 95% (respectively) of the total fluence (Kouveliotou et al. 1993; Koshut et al. 1996). Uncertainties in the peak flux, fluence, and durations are derived from the uncertainties in \tilde{P} , $\tilde{\nu}$, and the measured (background subtracted) count rates using the standard techniques for the propagation of small random errors (although the assumptions required by this method are not always satisfied).

We have attempted to ascertain how well the above procedures estimate burst intensities and directions by applying our methods to GRBs from the 3B catalog (Meegan et al. 1996). Because the burst intensities and directions must be estimated simultaneously by folding a model through the detector and atmospheric response matrices, systematic errors in the inferred quantities can arise from the background subtraction, the modeling of the event spectrum, spectral changes during the event, and detector calibration.

To evaluate the accuracy of our intensity measurements, we applied our analysis procedure to 29 GRBs from the 3B catalog (Meegan et al. 1996). We compared our peak fluxes (derived from the DISCLA data) to those obtained by the BATSE team (using the high resolution burst data types; see Pendleton et al. 1996). In 13 bursts the two measurements agreed to within the 1σ statistical uncertainties, and in 24 bursts they agreed to within 2σ . The largest disagreements (in terms of standard deviations) occur only in the most intense bursts, where the systematic errors are expected to dominate the statistical uncertainties. In those cases, the measurements disagree

by less than 30%.

At least two sources of systematic errors are responsible for the differences between our peak flux measurements (on intense bursts) and those obtained by Pendleton et al. (1996) for the 3B catalog. First, we model the incident photon spectrum as a power law, whereas Pendleton et al. (1996) allow for some curvature in the spectrum. Second, our peak flux measurement on the 1024 ms time scale is based on the DISCLA time bin that contains the most counts above background. The phase of this 1024 ms bin relative to the “true” 1024 ms peak flux depends on the DISCLA sampling times; therefore, the “true” 1024 ms peak flux could be spread over two DISCLA time bins. In contrast, Pendleton et al. (1996) use data with 64 ms time resolution to find which placement of a 1024 ms interval yields the highest peak flux on that time scale.

A similar procedure was used to assess the accuracy of our direction estimates. Comparison of a sample of GRBs from the 3B catalog and hard solar flares which triggered onboard suggests that an additional systematic uncertainty of about 4° should be added in quadrature to our statistical direction uncertainties for events with emission between 50 and 300 keV. This is expected since our version of the LOCBURST code roughly corresponds (with minor improvements) to the version used to produce the BATSE 1B catalog (Fishman et al. 1994b). The improvements to LOCBURST that reduced systematic errors to 1.6° for the 3B catalog require more spectral information than is available in the DISCLA data and have not been incorporated into the analysis described in this paper. For the channel 1 only (25–50 keV) events, comparison with solar flares indicates that the additional systematic uncertainty is about 6° .

For faint events the background subtraction can be a substantial source of systematic error because it is not always clear what is background and what is low-level emission before or after the event. The duration estimates (and thus fluence estimates) are particularly sensitive to the choice of background intervals (see Koshut et al. 1996).

5. Results

We have applied the search and analysis procedures described in sections 2 and 4 to the DISCLA data taken between 1993 January 13 and 1993 December 24. The corresponding range of Truncated Julian Day

numbers is TJD 9001–9345 (TJD = Julian Day – 2,440,000.5). Figure 7 shows a sky map which combines events from the GRB candidate (\diamond), solar flare ($*$), and unknown ($+$) categories. The concentration of solar events in the ecliptic plane is clearly visible, as is a concentration of low-energy ($+$) events in the vicinity of Cyg X-1 ($\ell = 71.3^\circ$, $b = 3.0^\circ$).

5.1. Gamma ray burst candidates

Our search so far yields 91 non-triggered GRB candidates. Tables 3 and 4 together are a catalog of these events.

The first column of Table 3 is a name which specifies the approximate time of the event in the format NTB *yyymmdd.ff*, where *yy* is the year, *mm* is the month, and *dd.ff* is the day. The second column gives the time of the laboratory trigger expressed as the TJD and the seconds of day (SOD). The next three columns give the estimated source direction in equatorial (J2000) coordinates and its associated statistical uncertainty. The full 1.0σ uncertainty in the direction estimates is obtained by combining the statistical uncertainty and the 4° systematic uncertainty (see section 4) in quadrature. The next column gives the largest value (among the three time scales in Table 1) of C_{max}/C_{min} , which is the ratio of the maximum count rate achieved during the event to the minimum count rate required for detection in the 50–300 keV band. Events with $C_{max}/C_{min} < 1.0$ were detected in the “catch-all” search of the 25–300 keV band (search “c” of Table 1) and may represent spectrally softer GRBs that had too few counts to trigger in the 50–300 keV band. The next column gives the threshold number of counts in the 50–300 keV band, C_{min} , and (in superscript) the search time scale which yielded the largest value of C_{max}/C_{min} . The next column lists the searches from Table 1 in which the event was detected.

The last column of Table 3 gives the reasons in our estimation why the events did not trigger onboard the spacecraft. The notation “R” indicates the event occurred during the readout of a previous onboard trigger. “D” indicates that the event occurred while the onboard trigger was disabled due to passage through a region with a high probability of magnetospheric particle precipitation events. “F” indicates that the event was too faint to meet the onboard burst trigger threshold. “BB” indicates that the event failed to trigger onboard because it biased the onboard background average. In one case, no experiment house-

keeping data were available so the state of the onboard trigger at the time of the event could not be determined. A “?” is entered for this event because we cannot determine whether the reason is “D” or “BB”. (See below for further discussion of these reasons and examples of events in each category.)

Table 4 gives the durations and intensities (in physical units) of the GRB candidates. The first column gives the name of the GRB candidate. The next two columns give estimates of the T_{50} and T_{90} duration measures. Events with no entry in the T_{50} column had their T_{90} duration estimated by eye. Uncertainties listed as 0.00 indicate that the uncertainty is less than the duration of one DISCLA time bin (1.024 s). The next column gives the peak flux in the 50–300 keV range as measured on the 1024 ms time scale. The next column gives the 50–300 keV fluence estimate.

Figure 8 shows a sky map of the direction estimates for the 91 untriggered GRB candidates. Events are shown as 1.0σ error circles centered on the best-fit location. Using the sky exposure calculated in section 3.1, the dipole and quadrupole moments of this direction distribution in Galactic coordinates are $\langle \cos \theta \rangle = -0.001 \pm 0.025$ and $\langle \sin^2 b - 1/3 \rangle = -0.022 \pm 0.021$, where θ is the angle between the burst direction and the Galactic center and b is the Galactic longitude. These values are consistent with the values $\langle \cos \theta \rangle = 0.00 \pm 0.06$ and $\langle \sin^2 b - 1/3 \rangle = 0.00 \pm 0.03$ expected from an isotropic distribution with the same number of bursts.

The dipole and quadrupole moments (corrected for sky exposure) with respect to equatorial coordinates are $\langle \sin \delta \rangle = 0.036 \pm 0.027$ and $\langle \sin^2 \delta - 1/3 \rangle = 0.074 \pm 0.024$. The dipole moment is consistent with that expected from an isotropic distribution, $\langle \sin \delta \rangle = 0.00 \pm 0.06$. The quadrupole moment appears to be only marginally consistent with the value $\langle \sin^2 \delta - 1/3 \rangle = 0.00 \pm 0.03$ expected for an isotropic distribution, indicating a weak concentration of events in the direction of the celestial poles. This result may be due to our tendency to classify GRBs with directions consistent with the sun as hard solar flares (see section 4).

The durations based on the T_{90} interval of these events range from $\lesssim 1.024$ s to ~ 350 s. We have examined the non-triggered GRB candidates to see if any appear to be related to an onboard triggered GRB that occurred within 1 day of a non-triggered event. In a combined sample of 91 non-triggered GRB can-

didates and 333 bursts from the 3B catalog (covering TJD 8995–9347), we found 7 pairs of bursts occurring within 1 day of each other and having direction measurements compatible within 1σ uncertainties. Only 3 of these 7 pairs involved a non-triggered GRB candidate. We do not consider this to be evidence that any of these pairs share the same burst source. We expect statistically to find 5–8 such pairs in a sample of the same size drawn from bursts randomly distributed uniformly in time and isotropically in space, with median location measurement errors of 8–10°. If one or more convincing pairs had been identified, however, they could have either been interpreted as burst repetition (see Wang 1994) or as bursts that extend knowledge of the T_{90} distribution to longer durations.

Figure 9 shows the integral peak flux distribution on the 1024 ms time scale for the untriggered GRB candidates. These events are concentrated at the faint end of the distribution, as expected for events which were generally too faint to cause an onboard trigger. When the non-triggered bursts are added to the triggered bursts for the same time period, the departure from the $-3/2$ power law slope expected from a homogeneous distribution (in Euclidean space) remains evident.

The top two panels of Figure 10 show the differential, $n(P)$, and integral, $N(> P)$, distributions of the peak fluxes, P , for the combined sample of 83 non-triggered GRB candidates and 233 onboard triggered GRBs that were detected on the 1024 ms time scale. The bottom panel shows the slope of the logarithmic number versus peak flux distribution, defined by

$$s(P) = \frac{d \log N(> P)}{d \log P} = -P \frac{n(P)}{N(> P)}. \quad (4)$$

The dotted histograms in Figure 10 show the distributions corrected for our laboratory trigger efficiency (see figure 3). The logarithmic slope $s(P)$ is consistent with a value of -0.5 ± 0.1 at peak fluxes of 0.15–0.35 ph cm⁻² s⁻¹.

Another measure of the inhomogeneity of the source distribution is reflected in the distribution of the V/V_{max} statistic for these events, given by $(C_{max}/C_{min})^{-3/2}$ (Schmidt, Higdon, & Heuter 1988). For the 91 non-triggered GRB candidates, the average value $\langle V/V_{max} \rangle = 0.28 \pm 0.03$. This value is biased by the elimination of the strong (triggered) bursts; but it is of interest when considering how biases inherent in the onboard trigger mechanism could affect conclusions about the

spatial inhomogeneity of GRB sources. For example, if the onboard trigger’s bias against slow-risers had significantly biased the value of $\langle V/V_{max} \rangle = 0.33 \pm 0.01$ obtained for the 3B catalog (Meegan et al. 1996) then the value obtained from the non-triggered GRB candidates alone could be expected to be much higher. For comparison, the value obtained using the cataloged bursts detected during the same time period is $\langle V/V_{max} \rangle = 0.13 \pm 0.02$. For the *combined* non-triggered GRB candidates and cataloged bursts, $\langle V/V_{max} \rangle = 0.18 \pm 0.02$.³

Figure 11 shows intensity profiles of some representative GRB candidates. Two adjacent plots are shown for each event. The plots on the left show the burst profile from the detector most brightly illuminated by the burst. The plots on the right show the profile from the second most illuminated (or “second brightest”) detector; they illustrate why some of the events did not cause an onboard burst trigger. The dashed lines show our estimate, B_k^{fit} of the background counts in each bin (k) based on polynomial fits to data before and after the event. The dotted lines show the $5.5\sigma_B$ threshold level given by $5.5\sqrt{B_k^{\text{fit}}}$. This level represents an “ideal” threshold estimate and it is in general different from the actual onboard background estimate that was in effect at the time the event occurred (see section 2). The onboard background estimate has a statistical uncertainty resulting from the uncertainty in the mean count rate during the 17.408 s background accumulation interval. The dot-dashed line represents the threshold corresponding to $5.5\sqrt{B_k^{\text{fit}}}$ plus the uncertainty in the onboard trigger level arising from the onboard background uncertainty. An event with peak counts just slightly above our “ideal” $5.5\sigma_B$ threshold may fall below the onboard burst trigger threshold even though both thresholds are based on background estimates that are statistically consistent with each other. We classify events with peak counts less than $5.5\sqrt{B_k^{\text{fit}}}$ plus the onboard threshold uncertainty as too faint to trigger onboard (“F” in table 3).

The event in row (a) of Figure 11 failed to trigger onboard because it occurred during the read out period of a previous onboard burst trigger. The event in row (b) occurred while the onboard burst trigger

was disabled due to spacecraft passage through a region identified with a high probability of a false trigger due to atmospheric electron precipitation events. The events in rows (c) and (d) failed to trigger onboard because the onboard background estimate was biased upwards by slowly rising burst flux; these are examples of slow-risers. Panels (e) and (f) show events that were too faint to meet the onboard trigger threshold.

We estimate that the 91 GRB candidates failed to trigger onboard the spacecraft for the following reasons: 15 events occurred during the read out of a brighter event, 2 occurred while the onboard trigger was disabled for other reasons, 63 were below the $5.5\sigma_B$ threshold in the second brightest detector, and 10 had a slow rise that modified the onboard background estimate. One occurred during a time for which no spacecraft housekeeping data are available to determine the status of the onboard trigger.

The onboard trigger mechanism’s bias against slow-rising GRBs has been discussed by Lingenfelter and Higdon (1996). The 10 (possibly 11) events we find that failed to trigger onboard the spacecraft *solely* because of the slow-rising effect constitute 3.0% (possibly 3.3%) of the total 332 GRBs that have been detected above the onboard threshold while the trigger was active. This is a lower fraction than estimated elsewhere (Lingenfelter & Higdon 1996). We note, however, that our search algorithm is biased against faint events which rise on time scales longer than ~ 30 s on the 1.024 s time scale (see Figure 6).

5.2. Unknown events

The “unknown” category of laboratory triggers includes all events which were not obviously of terrestrial or solar origin and which do not resemble a GRB. Most of the channel 1 only (low-energy, 25–50 keV) events fall into this category. The major problem with this class of events is that it is dominated by intensity fluctuations from Cyg X-1: of 799 events in the unknown category, 689 are consistent with this source (although they may not *all* be from Cyg X-1); see the clustering of events marked (+) in Figure 7. If we remove all the events consistent with Cyg X-1 we are left with the sky map shown in Figure 12, where events are plotted as their 1.0σ error circles. Although Figure 12 shows some general clustering toward the galactic center, there is no obvious clustering that would indicate the activity of any particular source.

We find two events which can convincingly be at-

³These values are corrected from the erroneous values that appeared in earlier versions of this paper and in the version that appeared in ApJ, 491, 704 (1997). See erratum at end of paper.

tributed to SGR 1806–20 based on intensity, spectral softness, and location. Both occur within one day of the onboard triggered emission from SGR 1806–20 reported by Kouveliotou et al. (1994). Recent activity from this source suggests that more events from SGR 1806–20 (or other SGRs) may be detectable when this search is extended (Kouveliotou et al. 1996).

6. Conclusions

Our search of 345 days of archival BATSE data has uncovered a significant number of astronomically interesting transients.

The 91 non-triggered GRB candidates detected (so far) by this search include some of the faintest GRBs ever observed. When combined with the bursts detected by the onboard trigger during the same 345 days, these events extend knowledge of the peak flux distribution to values a factor of ~ 2 lower than the onboard detection threshold. Near the onboard trigger threshold, the combined sample is expected to be nearly complete (on the 1024 ms time scale). We find the logarithmic slope of the integral number versus peak flux distribution to be -0.5 ± 0.1 at peak fluxes of $0.15\text{--}0.35 \text{ ph cm}^{-2} \text{ s}^{-1}$ after correcting for our laboratory trigger efficiency. The value of $\langle V/V_{max} \rangle = 0.18 \pm 0.02$ for the combined sample.⁴ We find no evidence for anisotropy in the direction distribution of these events.

These results are consistent with those obtained from analyses of the published BATSE catalogs. The biases inherent in the onboard trigger mechanism do not appear to have significantly undermined its sampling of GRBs, at least for bursts with the characteristics our search can detect.

The non-triggered GRB candidates add to the database of GRBs available for duration studies, searches for burst repetition, and searches for gravitational lensing (see Fishman & Meegan 1995 for an overview and references). The slow-risers and the more intense bursts (which occurred while the onboard trigger was disabled) will probably be the most useful non-triggered GRBs for such purposes.

The low-energy (25–50 keV) events detected by our search arise from a variety of sources. While intensity fluctuations from Cyg X-1 dominate this class

of events, we find a significant number that must be due to other sources. Because of the difficulty in accurately estimating the source directions of these events, identification of the individual sources responsible for them depends on unique repetition patterns or temporal coincidences with other observations (as in the case of events from SGR 1806–20). The possibility remains that we may identify among these events new source activity or completely new burst sources.

The effort to extend this search to cover the more than 5 years of remaining archival data is in progress.

J. M. K. acknowledges support from a National Science Foundation Graduate Research Fellowship during the preliminary phase of this research and subsequent support from NASA Graduate Student Researchers Program Fellowship NGT8-52816. W. H. G. L. acknowledges support from NASA under grant NAG5-3804. C. K. acknowledges support from NASA under grant NAG5-2560. J. v. P. acknowledges support from NASA under grant NAG5-2755. We also thank Scott Barthelmy and James Kuyper for sharing the BACODINE version of the BATSE LOCBURST code, which formed the foundation for our trigger efficiency and burst location algorithms.

⁴This value is corrected from the erroneous value that appeared previously. See erratum at end of paper.

ERRATUM

In the paper “A Search for Nontriggered Gamma-ray Bursts in the BATSE Data Base” by Kommers et al. (ApJ, 491, 704, [1997]) the values of $\langle V/V_{max} \rangle$ that include onboard-triggered bursts are incorrect. Owing to a programming error, whenever a value of C_{min} was available for a burst listed in the 4B catalog, that catalog value (appropriate for the onboard burst trigger) overwrote the value appropriate for our more sensitive off-line search. Thus the values of V/V_{max} were overestimated by a factor of $\sim 2^{3/2}$ for the bursts that were triggered onboard. This error does *not* affect the values of C_{max}/C_{min} and C_{min} for the non-triggered GRBs listed in Table 3, nor does it affect the value of $\langle V/V_{max} \rangle = 0.28 \pm 0.03$ computed for the non-triggered (only) GRB sample.

The correct value of $\langle V/V_{max} \rangle$ for the onboard-triggered bursts detected by our off-line search is $\langle V/V_{max} \rangle = 0.13 \pm 0.02$. For the *combined* non-triggered GRB candidates and onboard-triggered bursts, $\langle V/V_{max} \rangle = 0.18 \pm 0.02$. This value is significantly lower than the value of $\langle V/V_{max} \rangle = 0.33 \pm 0.01$ obtained for the 3B catalog. These corrections, therefore, significantly *strengthen* the conclusion of the paper, that the BATSE onboard trigger has *not* missed a significant population of faint gamma-ray bursts owing to the biases inherent in the onboard burst trigger mechanism.

REFERENCES

- Briggs, M. S. 1995, *Ap&SS*, 231, 1
- Brock, M. N., Meegan, C. A., Fishman, G. J., Wilson, R. B., Paciasas, W. S., & Pendleton, G. N. 1991, in *AIP Conf. Proc. 265, Gamma Ray Bursts*, eds. W. S. Paciasas & G. J. Fishman (New York: AIP), 399
- Burgess, W. C. & Inan, U. S. 1993, *J. Geophys. Res.*, 98, 15643
- Fishman, G. J., et al. 1989, *Proceedings of the GRO Science Workshop*, 2-39
- Fishman, G. J., et al. 1994, *Science*, 264, 1313
- Fishman, G. J., et al. 1994, *ApJS*, 92, 229
- Fishman, G. J., & Meegan, C. A. 1995, *ARA&A*, 33, 415
- Hartmann, D. H. 1995, *A&A Rev.*, 6, 225
- Horack, J. M., Fishman, G. J., Meegan, C. A., Wilson, R. B., & Paciasas, W. S. 1992, in *AIP Conf. Proc. 265, Gamma Ray Bursts*, eds. W. S. Paciasas & G. J. Fishman (New York: AIP), 373
- Kommers, J. M., Lewin, W. H. G., Van Paradijs, J., Kouveliotou, C., Fishman, G. J., & Briggs, M. S. 1996, in *AIP Conf. Proc. 384, Gamma Ray Bursts*, eds. C. Kouveliotou, M. S. Briggs, & G. J. Fishman (New York: AIP), 441
- Koshut, T. M., Paciasas, W. S., Kouveliotou, C., van Paradijs, J., Pendleton, G. N., Fishman, G. J., & Meegan, C. A. 1996, *ApJ*, 463, 570
- Kouveliotou, C. et al. 1993, *ApJ*, 413, L101
- Kouveliotou, C., et al. 1994, *Nature*, 368, 125
- Kouveliotou, C., Fishman, G. J., Meegan, C. A., van Paradijs, J., Briggs, M. S., Richardson, G., & Hurley, K. 1996, *IAU Circ.*, No. 6501
- Lingenfelter, R. E., & Higdon, J. C. 1996, in *AIP Conf. Proc. 366, High Velocity Neutron Stars and Gamma Ray Bursts*, eds. R. E. Rothschild & R. E. Lingenfelter (New York: AIP), 164
- Meegan, C. A., et al. 1996, *ApJS*, 106, 65
- Meegan, C. A., Fishman, G. J., Wilson, R. B., Paciasas, W. S., Pendleton, G. N., Horack, J. M., Brock, M. N., & Kouveliotou, C. 1992, *Nature*, 355, 143
- Pendleton, G. N., et al. 1995, *Nuclear Instruments & Methods in Physics Research A*, 364, 567
- Pendleton, G. N., et al. 1996, *ApJ*, 464, 606
- Rubin, B. C., Horack, J. M., Brock, M. N., Meegan, C. A., Fishman, G. J., Wilson, R. B., Paciasas, W. S., & Van Paradijs, J. 1993, in *AIP Conf. Proc. 280, Compton Gamma Ray Observatory*, eds. M. Friedlander, N. Gehrels, & D. J. Macomb (New York: AIP), 719
- Schmidt, M., Higdon, J. C., & Heuter, G. 1988, *ApJ*, 329, L85
- Skelton, R. T., & Mahoney, W. A. 1994, in *AIP Conf. Proc. 307, Gamma Ray Bursts*, eds. G. J. Fishman, J. J. Brainerd, & K. Hurley (New York: AIP), 706
- Tegmark, M. 1996, *ApJ*, 470, L81
- Wang, V. C. 1994, Ph. D. Thesis, University of California at San Diego
- Young, C. A., Arndt, M. B., Biesecker, D. A., & Ryan, J. M. 1996, in *AIP Conf. Proc. 384, Gamma Ray Bursts*, eds. C. Kouveliotou, M. S. Briggs, & G. J. Fishman (New York: AIP), 555
- Van Paradijs, J., et al. 1993, in *AIP Conf. Proc. 280, Compton Gamma Ray Observatory*, eds. M. Friedlander, N. Gehrels, & D. J. Macomb (New York: AIP), 877

Fig. 1.— Schematic diagram of the laboratory (off-line search) trigger criteria. If the significances of the fluctuations measured in the two most brightly illuminated detectors lie in the non-shaded area A , our search will flag that time bin as a laboratory trigger.

Fig. 2.— Integral distribution of $S_d(k)$ for the data of May 27, 1993 (TJD 9135) in detector 0. The dotted line shows the expectation for a Gaussian distribution with zero mean and unit variance. The excess counts are attributed both to deficiencies in the background estimate and to the activity of real sources.

Fig. 3.— Off-line trigger efficiency. The solid line shows the efficiency of our off-line search algorithm for detecting an event with a given peak flux in the 50–300 keV range on the 1024 ms time scale. The long-dashed line shows the trigger efficiency for our off-line search on the 4096 ms time scale. The short-dashed line shows the trigger efficiency from the 1B catalog.

Fig. 4.— Sky exposure for our 50-300 keV off-line trigger search as a function of declination, assuming a search spanning 345 days.

Fig. 5.— Simplified profile of a “slow-riser”. It reaches maximum significance s by rising with a slope r given in sigmas per second.

Fig. 6.— Contours showing the probability of detecting a “slow-riser” with a given peak significance (relative to the “true” background) and a given slope. Thick contours apply to our off-line search algorithm, and thin contours apply to the onboard burst trigger.

Fig. 7.— Sky map of all non-terrestrial non-triggered events in Galactic coordinates. The GRB candidate (\diamond), solar flare ($*$), and unknown ($+$) categories are shown. The concentration of solar events in the ecliptic plane is clearly visible, as is a concentration of low-energy ($+$) events in the vicinity of Cyg X-1 ($\ell = 71^\circ.3$, $b = 3^\circ.0$).

Fig. 8.— Sky map of 91 non-triggered GRB candidates, shown as 1σ error circles in Galactic coordinates.

Fig. 9.— Integral number versus peak flux distribution of 91 non-triggered GRB candidates (dotted line). No corrections for trigger efficiency have been applied. The distribution for GRBs from the 3B catalog detected during the same time period is also shown (dashed line), as is that for the combined sample (solid line).

Fig. 10.— Peak flux distributions for 83 non-triggered GRB candidates combined with the 233 onboard triggered events (1024 ms time scale) from the same time period. The solid histogram shows the observed numbers and the dotted histogram shows the numbers corrected for laboratory trigger efficiency. $n(P)$ is the differential distribution, $N(P)$ is the integral distribution, and $s(P)$ is the slope of the logarithmic number versus peak flux distribution.

Fig. 11.— Intensity profiles of selected GRB candidates. Two panels are used for each event. Those on the left represent the count rates observed in the detector most brightly illuminated by the burst. Those on the right represent the count rates in the second most illuminated detector. Dashed lines represent our background estimate derived from polynomial fits to data before and after the event. Dotted lines represent an “ideal” onboard trigger threshold based on our background estimates; the actual onboard trigger threshold is in general different and is based on an average count rate that is recomputed every 17.408 s. The dot-dashed line represents the “ideal” onboard threshold *plus* the uncertainty arising from the statistical uncertainty in onboard background average. The burst in row (a) occurred during the read out period of a more intense event, and that in row (b) occurred while the onboard trigger was disabled. The bursts in rows (c) and (d) modified the onboard background average. Rows (e) and (f) show events that were too faint cause an onboard burst trigger.

Fig. 12.— Low-energy (25–50 keV) events plotted as 1σ error circles in Galactic coordinates (those consistent with Cyg X-1 excluded).

TABLE 1
PARAMETERS OF THE TIME SERIES FORMED FROM THE DISCLA DATA (SEE TEXT).

Search	Time Bin Duration (s)	Energy Channels	M	Σ	N_b	Statistical Detections per day
a	1.024	1	2.5	4.0	20	0.021
b	1.024	2+3	2.5	4.0	20	0.021
c	1.024	1+2+3	2.5	4.0	20	0.021
d	4.096	1	2.5	4.0	15	0.005
e	4.096	2+3	2.5	4.0	15	0.005
f	8.192	1	2.5	4.0	5	0.002
g	8.192	2+3	2.5	4.0	5	0.002

TABLE 2

CLASSIFICATION MATRIX OF 317 ONBOARD TRIGGERS THAT WERE ALSO DETECTED BY OUR OFF-LINE SEARCH.
 ROWS INDICATE THE CLASSIFICATION ASSIGNED BY THE BATSE TEAM, AND COLUMNS INDICATE THE
 CLASSIFICATION ASSIGNED BY US (SEE TEXT).

	Off-line GRB Candidate	Off-line Solar Flare	Off-line Magnetospheric	Off-line Other
BATSE GRB	198	10	4	9
BATSE Solar Flare	0	50	3	0
BATSE Magnetospheric	2	2	30	4
BATSE Unclassified	0	0	0	5

TABLE 3

TIMES, SOURCE DIRECTIONS, C_{max}/C_{min} , SEARCHES TRIGGERED, AND REASONS FOR ELUDING THE ONBOARD TRIGGER FOR 91 NON-TRIGGERED GRB CANDIDATES.

Name	Time (TJD:s)	RA (°)	Dec (°)	Err. (°)	$\frac{C_{max}}{C_{min}}$	C_{min}	Searches Triggered	Reason Non-triggered
NTB 930118.74	9005:64425.6	219.3	-32.9	0.5	31.0	349 ⁴	abcdefg	R
NTB 930211.88	9029:76428.9	285.5	20.0	7.7	3.5	425 ⁸	bcdefg	F
NTB 930216.63	9034:54956.7	42.5	-8.7	3.6	2.6	447 ⁸	bcdeg	F
NTB 930217.80	9035:69525.6	311.7	-12.0	28.2	0.9	286 ⁴	c	F
NTB 930225.86	9043:75141.2	336.6	35.2	38.4	1.1	155 ¹	abc	F
NTB 930227.83	9045:71910.5	241.2	81.0	11.0	2.1	377 ⁸	ceg	F
NTB 930228.85	9046:73728.6	18.6	2.5	8.3	2.2	477 ⁸	g	F
NTB 930302.20	9048:17613.4	214.1	42.5	6.2	2.4	483 ⁸	g	F
NTB 930303.65	9049:56726.7	0.0	-50.8	3.3	3.2	501 ⁸	bceg	F
NTB 930305.70	9051:60923.0	275.2	59.8	3.5	3.2	330 ⁸	bceg	F
NTB 930307.54	9053:46677.1	94.2	-15.5	12.7	1.7	411 ⁸	bc	F
NTB 930308.30	9054:26710.7	88.7	-31.6	3.5	3.8	399 ⁸	bceg	F
NTB 930310.08	9056: 7334.5	333.5	-57.2	5.0	2.6	321 ⁸	abcdefg	F
NTB 930315.46	9061:40070.8	232.5	-32.1	3.9	2.0	395 ⁸	g	F
NTB 930316.74	9062:64295.0	314.1	-87.1	19.8	1.6	132 ¹	bc	F
NTB 930318.18	9064:15764.1	16.2	44.0	8.9	2.4	425 ⁸	bceg	F
NTB 930320.94	9066:81767.0	228.3	72.7	15.5	7.2	436 ⁸	bcefg	R
NTB 930325.65	9071:56254.1	46.9	46.8	5.8	2.8	383 ⁸	bceg	F
NTB 930327.46	9073:40594.6	178.7	-5.5	13.2	3.4	553 ⁸	bc	F
NTB 930330.91	9076:79132.8	109.2	-54.4	2.0	1.7	481 ⁸	cfg	F
NTB 930403.84	9080:73239.2	245.8	-59.6	6.2	3.0	351 ⁸	abcdefg	BB
NTB 930409.13	9086:11442.8	315.6	68.8	4.0	3.3	334 ⁸	abcdef	BB
NTB 930409.91	9086:78639.7	275.4	-17.7	0.9	12.8	501 ⁸	abcdefg	R
NTB 930410.76	9087:65711.8	182.3	-45.3	7.3	3.0	380 ⁸	abcefg	F
NTB 930416.56	9093:48602.2	115.6	-21.0	6.2	3.1	389 ⁸	abcdefg	F
NTB 930417.78	9094:68020.4	190.5	8.3	6.7	1.7	351 ⁸	abcdf	F
NTB 930421.11	9098:10164.9	23.7	19.3	7.0	2.0	520 ⁸	g	F
NTB 930422.58	9099:50820.2	50.4	-7.5	2.1	4.9	315 ⁸	bc	?
NTB 930424.45	9101:38903.4	230.3	-55.7	0.4	21.2	523 ⁸	abcde	D
NTB 930424.97	9101:84156.0	254.1	68.6	3.2	3.5	332 ⁸	abcefg	BB
NTB 930426.48	9103:41832.1	33.2	-81.9	5.4	4.4	133 ¹	abcdefg	R
NTB 930427.59	9104:51155.6	60.1	34.3	11.5	2.2	453 ⁸	abd	F
NTB 930429.75	9106:65094.3	35.7	-25.8	5.4	5.7	344 ⁸	bcdefg	BB
NTB 930501.34	9108:29834.4	181.4	-32.9	31.7	1.1	114 ¹	ab	F
NTB 930506.63	9113:55244.4	259.8	35.4	8.4	2.4	548 ⁸	cg	F
NTB 930508.95	9115:82814.6	82.9	41.4	7.6	3.4	494 ⁸	bce	D
NTB 930513.98	9120:85533.8	169.0	12.0	39.5	1.5	384 ⁸	bc	F
NTB 930519.39	9126:34288.8	272.4	-24.2	83.8	1.4	134 ¹	bc	F
NTB 930612.63	9150:55165.1	254.5	34.3	2.9	12.1	277 ⁴	abcde	R
NTB 930616.27	9154:23806.6	179.5	1.8	4.4	11.7	165 ¹	abcde	R
NTB 930617.23	9155:20027.0	244.9	-12.7	6.1	2.5	299 ⁸	bceg	F
NTB 930626.94	9164:81935.0	342.6	-34.9	3.3	3.6	512 ⁸	bcdefg	BB
NTB 930630.71	9168:61420.2	70.0	38.1	6.9	3.0	438 ⁸	bcdeg	F
NTB 930701.62	9169:54302.9	226.4	39.4	2.5	4.2	338 ⁸	abcde	F
NTB 930705.64	9173:55983.3	195.3	-59.5	7.2	2.0	334 ⁸	bcefg	F
NTB 930717.20	9185:18101.4	184.3	57.8	10.3	1.5	364 ⁴	bcd	F
NTB 930717.98	9185:85357.7	200.5	-66.4	3.5	3.3	374 ⁸	abc	F
NTB 930722.84	9190:73297.6	310.5	-48.2	3.5	2.1	412 ⁸	eg	F
NTB 930728.54	9196:47072.9	90.8	19.0	21.0	3.3	510 ⁸	d	R
NTB 930804.71	9203:61858.5	32.7	66.6	5.0	3.7	317 ⁸	bcefg	F
NTB 930811.62	9210:53728.4	347.5	65.0	3.6	2.9	325 ⁸	bc	F
NTB 930812.27	9211:23904.9	198.0	-27.8	2.4	4.9	409 ⁸	bcdef	BB
NTB 930813.76	9212:65850.5	76.9	77.1	8.1	3.7	336 ⁸	abcdefg	F
NTB 930816.67	9215:58569.4	155.1	53.8	5.9	3.5	429 ⁸	bceg	F
NTB 930820.76	9219:65885.3	62.7	36.4	7.6	2.8	386 ⁸	bceg	F
NTB 930821.64	9220:56096.9	148.0	-40.4	11.7	1.2	123 ¹	bc	F
NTB 930825.48	9224:41775.3	59.7	63.1	21.4	1.5	298 ⁴	cg	F
NTB 930827.60	9226:51963.0	349.4	68.5	19.0	2.5	506 ⁸	bceg	F
NTB 930902.45	9232:39001.8	224.2	20.8	6.6	2.1	364 ⁸	acg	F
NTB 930918.46	9248:39913.1	275.3	-81.0	11.8	2.6	310 ⁸	bceg	F
NTB 930921.84	9251:73133.2	75.0	-35.7	25.2	1.3	292 ⁸	bce	F
NTB 930924.37	9254:32251.0	98.1	-9.6	21.5	3.3	403 ⁸	bcde	F
NTB 930928.93	9258:81199.3	260.5	-67.6	10.4	2.2	529 ⁸	bef	F
NTB 930928.94	9258:81393.3	79.8	45.2	7.0	1.7	329 ⁸	f	F
NTB 931001.06	9261: 5859.5	207.2	12.6	1.4	5.6	582 ⁸	abcde	R
NTB 931001.72	9261:62917.3	8.5	12.5	2.2	3.4	473 ⁸	bcefg	BB
NTB 931007.20	9267:17771.7	311.3	-5.2	23.7	2.2	368 ⁸	bg	F
NTB 931007.33	9267:29319.3	355.1	36.4	48.7	1.7	363 ⁸	bg	F

TABLE 3—*Continued*

Name	Time (TJD:s)	RA ($^{\circ}$)	Dec ($^{\circ}$)	Err. ($^{\circ}$)	$\frac{C_{max}}{C_{min}}$	C_{min}	Searches Triggered	Reason Non-triggered
NTB 931008.05	9268: 5024.9	26.4	-65.6	30.5	1.2	190 ¹	bc	F
NTB 931008.63	9268:54916.8	42.3	42.8	3.7	4.7	492 ⁸	ceg	BB
NTB 931011.96	9271:83718.3	248.4	63.9	23.4	1.2	373 ⁴	bc	F
NTB 931014.08	9274: 7552.2	65.5	72.0	55.6	1.5	148 ¹	bc	F
NTB 931017.22	9277:19221.7	185.7	-67.5	18.3	1.8	448 ⁸	b	F
NTB 931020.10	9280: 8697.5	285.0	16.0	14.0	1.7	447 ⁸	c	F
NTB 931025.93	9285:80462.5	173.2	15.9	4.8	2.7	438 ⁸	bceg	F
NTB 931031.23	9291:20519.6	173.2	63.4	17.2	3.0	163 ¹	bce	R
NTB 931106.48	9297:42228.4	34.3	69.7	3.7	3.7	406 ⁸	bcefg	BB
NTB 931106.90	9297:78310.6	185.7	-38.0	16.1	2.7	279 ⁴	bc	R
NTB 931107.31	9298:26896.0	106.0	-27.7	12.6	2.9	578 ⁸	abcde	BB
NTB 931111.71	9302:61941.4	244.6	49.5	0.8	9.2	352 ⁸	abcdefg	R
NTB 931113.04	9304: 3669.7	50.9	-40.2	10.1	2.1	383 ⁸	bce	F
NTB 931115.77	9306:66557.6	279.1	27.9	11.0	3.1	401 ⁴	abceg	R
NTB 931125.86	9316:74847.4	177.7	-77.4	2.4	12.0	529 ⁸	abcdefg	R
NTB 931206.45	9327:39631.5	174.1	-14.7	15.0	3.1	404 ⁸	bceg	F
NTB 931209.89	9330:77266.1	20.0	-37.4	3.0	3.3	443 ⁸	bceg	F
NTB 931215.12	9336:10491.5	326.0	-3.5	12.2	2.3	298 ⁴	abd	F
NTB 931220.16	9341:13826.7	120.2	45.7	8.5	3.0	414 ⁸	bce	F
NTB 931220.73	9341:63345.3	50.0	22.0	3.9	7.3	435 ⁸	abcdefg	R
NTB 931222.11	9343:10361.5	278.9	29.5	5.4	1.9	565 ⁸	g	F
NTB 931222.82	9343:70972.1	209.6	-35.5	14.8	6.2	178 ¹	abceg	R
NTB 931223.07	9344: 6589.6	212.8	40.0	23.2	1.5	200 ¹	bc	F

TABLE 4
DURATIONS AND INTENSITIES OF NON-TRIGGERED GRB CANDIDATES.

Name	T_{50} (s)	T_{90} (s)	Peak Flux ($\text{ph cm}^{-2} \text{s}^{-1}$)	Fluence (ergs cm^{-2})
NTB 930118.74	2.05 ± 0.00	4.10 ± 0.00	4.53 ± 0.14	(3.00 ± 0.19)E-6
NTB 930211.88	19.46 ± 2.90	58.37 ± 6.23	0.26 ± 0.05	(8.46 ± 1.95)E-7
NTB 930216.63	23.55 ± 0.00	40.96 ± 8.44	0.28 ± 0.07	(6.34 ± 1.54)E-7
NTB 930217.80	...	3.07 ± 1.02	0.18 ± 0.10	(5.86 ± 3.50)E-8
NTB 930225.86	...	4.10 ± 1.02	0.18 ± 0.07	(7.72 ± 2.94)E-8
NTB 930227.83	37.89 ± 2.29	57.34 ± 7.24	0.17 ± 0.05	(5.46 ± 1.36)E-7
NTB 930228.85	26.62 ± 3.24	91.14 ± 16.67	0.16 ± 0.04	(9.25 ± 1.98)E-7
NTB 930302.20	21.50 ± 3.24	57.34 ± 15.50	0.26 ± 0.09	(1.44 ± 0.44)E-6
NTB 930303.65	32.77 ± 1.45	70.66 ± 7.17	0.20 ± 0.05	(7.64 ± 1.42)E-7
NTB 930305.70	5.12 ± 1.45	12.29 ± 1.45	0.59 ± 0.19	(8.88 ± 3.73)E-7
NTB 930307.54	5.12 ± 1.02	22.53 ± 16.79	0.18 ± 0.19	(2.26 ± 2.35)E-7
NTB 930308.30	18.43 ± 1.45	38.91 ± 2.29	0.43 ± 0.11	(2.18 ± 0.53)E-6
NTB 930310.08	10.24 ± 0.00	34.82 ± 23.57	0.35 ± 0.05	(4.16 ± 0.68)E-7
NTB 930315.46	15.36 ± 2.29	35.84 ± 4.22	0.23 ± 0.05	(7.61 ± 1.81)E-7
NTB 930316.74	...	3.07 ± 1.02	0.22 ± 0.07	(8.05 ± 2.47)E-8
NTB 930318.18	15.36 ± 2.05	35.84 ± 6.87	0.17 ± 0.04	(3.97 ± 0.94)E-7
NTB 930320.94	25.60 ± 0.00	59.39 ± 3.07	0.96 ± 0.15	(4.09 ± 0.62)E-6
NTB 930325.65	10.24 ± 1.45	20.48 ± 5.12	0.24 ± 0.06	(5.13 ± 1.42)E-7
NTB 930327.46	12.29 ± 3.69	46.08 ± 31.89	0.29 ± 0.07	(7.86 ± 2.88)E-7
NTB 930330.91	12.29 ± 2.29	52.22 ± 14.37	0.24 ± 0.06	(4.99 ± 1.47)E-7
NTB 930403.84	13.31 ± 0.00	92.16 ± 10.69	0.26 ± 0.04	(6.96 ± 0.93)E-7
NTB 930409.13	14.34 ± 1.02	39.94 ± 9.27	0.40 ± 0.05	(7.91 ± 1.20)E-7
NTB 930409.91	12.29 ± 1.02	53.25 ± 0.00	1.19 ± 0.06	(3.06 ± 0.34)E-6
NTB 930410.76	24.58 ± 1.02	74.75 ± 3.07	0.29 ± 0.05	(1.09 ± 0.16)E-6
NTB 930416.56	...	20.48 ± 5.12	0.21 ± 0.04	(3.54 ± 0.58)E-7
NTB 930417.78	5.12 ± 1.45	35.84 ± 26.62	0.21 ± 0.06	(2.05 ± 0.82)E-7
NTB 930421.11	47.10 ± 3.24	(1.29 ± 0.23)E+2	0.15 ± 0.04	(1.28 ± 0.26)E-6
NTB 930422.58	15.36 ± 1.02	44.03 ± 17.41	0.27 ± 0.03	(1.20 ± 0.13)E-6
NTB 930424.45	41.98 ± 1.02	(1.06 ± 0.03)E+2	1.28 ± 0.06	(1.38 ± 0.08)E-5
NTB 930424.97	12.29 ± 1.02	32.77 ± 15.36	0.33 ± 0.04	(8.77 ± 1.30)E-7
NTB 930426.48	...	3.07 ± 1.02	0.70 ± 0.10	(1.66 ± 0.27)E-7
NTB 930427.59	21.50 ± 1.45	46.08 ± 7.17	0.19 ± 0.06	(4.45 ± 1.30)E-7
NTB 930429.75	43.01 ± 1.45	(1.11 ± 0.15)E+2	0.38 ± 0.04	(2.24 ± 0.25)E-6
NTB 930501.34	...	2.05 ± 1.02	0.23 ± 0.14	(5.71 ± 3.59)E-8
NTB 930506.63	34.82 ± 8.26	82.94 ± 5.22	0.18 ± 0.05	(9.14 ± 2.73)E-7
NTB 930508.95	5.12 ± 1.45	22.53 ± 15.39	0.24 ± 0.05	(4.17 ± 1.39)E-7
NTB 930513.98	...	41.98 ± 10.24	0.17 ± 0.05	(3.67 ± 1.07)E-7
NTB 930519.39	...	1.02 ± 0.00	0.35 ± 0.29	(1.15 ± 0.96)E-7
NTB 930612.63	6.14 ± 2.05	50.18 ± 9.22	1.33 ± 0.08	(1.23 ± 0.42)E-6
NTB 930616.27	...	1.02 ± 0.00	3.21 ± 0.77	(7.97 ± 1.94)E-7
NTB 930617.23	51.20 ± 1.02	73.73 ± 5.12	0.29 ± 0.06	(1.35 ± 0.28)E-6
NTB 930626.94	14.34 ± 1.02	61.44 ± 38.01	0.27 ± 0.05	(8.29 ± 1.25)E-7
NTB 930630.71	...	18.43 ± 5.12	0.23 ± 0.05	(3.86 ± 0.71)E-7
NTB 930701.62	20.48 ± 1.02	35.84 ± 3.07	0.45 ± 0.05	(1.07 ± 0.14)E-6
NTB 930705.64	12.29 ± 1.02	48.13 ± 16.38	0.20 ± 0.05	(4.10 ± 0.95)E-7
NTB 930717.20	2.05 ± 1.45	3.07 ± 1.02	0.21 ± 0.09	(1.37 ± 1.11)E-7
NTB 930717.98	6.14 ± 1.45	17.41 ± 3.07	0.32 ± 0.05	(3.93 ± 1.09)E-7
NTB 930722.84	26.62 ± 2.29	72.70 ± 9.44	0.20 ± 0.05	(8.37 ± 1.62)E-7
NTB 930728.54	66.56 ± 15.22	(3.43 ± 0.21)E+2	0.29 ± 0.05	(3.60 ± 0.92)E-6
NTB 930804.71	19.46 ± 1.02	49.15 ± 16.42	0.25 ± 0.04	(9.05 ± 1.10)E-7
NTB 930811.62	18.43 ± 2.29	45.06 ± 4.22	0.29 ± 0.06	(7.27 ± 1.71)E-7
NTB 930812.27	28.67 ± 2.29	77.82 ± 3.24	0.39 ± 0.04	(1.97 ± 0.25)E-6
NTB 930813.76	(1.02 ± 0.02)E+2	(1.36 ± 0.02)E+2	0.29 ± 0.05	(1.16 ± 0.19)E-6
NTB 930816.67	8.19 ± 1.02	24.58 ± 4.10	0.33 ± 0.10	(6.95 ± 2.21)E-7
NTB 930820.76	7.17 ± 1.02	45.06 ± 23.55	0.22 ± 0.05	(4.03 ± 0.98)E-7
NTB 930821.64	...	2.05 ± 1.02	0.30 ± 0.10	(9.30 ± 3.26)E-8
NTB 930825.48	4.10 ± 2.29	20.48 ± 5.12	0.14 ± 0.06	(1.58 ± 1.07)E-7
NTB 930827.60	15.36 ± 3.07	48.13 ± 15.36	0.22 ± 0.07	(5.23 ± 1.80)E-7
NTB 930902.45	28.67 ± 10.69	74.75 ± 16.51	0.16 ± 0.04	(7.53 ± 3.05)E-7
NTB 930918.46	16.38 ± 4.10	54.27 ± 14.34	0.20 ± 0.05	(5.54 ± 1.95)E-7
NTB 930921.84	12.29 ± 3.24	56.32 ± 18.43	0.32 ± 0.12	(3.12 ± 1.47)E-7
NTB 930924.37	8.19 ± 1.02	28.67 ± 17.17	0.22 ± 0.05	(5.58 ± 1.23)E-7
NTB 930928.93	2.05 ± 1.02	4.10 ± 2.05	0.19 ± 0.06	(6.92 ± 4.24)E-8
NTB 930928.94	14.34 ± 1.45	28.67 ± 2.29	0.13 ± 0.04	(3.75 ± 1.04)E-7
NTB 931001.06	4.10 ± 0.00	12.29 ± 3.07	0.74 ± 0.08	(8.66 ± 0.93)E-7
NTB 931001.72	16.38 ± 2.29	82.94 ± 8.44	0.28 ± 0.06	(9.18 ± 1.98)E-7
NTB 931007.20	5.12 ± 1.02	35.84 ± 5.12	0.23 ± 0.07	(3.62 ± 1.27)E-7
NTB 931007.33	...	8.19 ± 4.10	0.43 ± 0.74	(4.94 ± 8.59)E-7

TABLE 4—*Continued*

Name	T_{50} (s)	T_{90} (s)	Peak Flux ($\text{ph cm}^{-2} \text{s}^{-1}$)	Fluence (ergs cm^{-2})
NTB 931008.05	...	2.05 ± 1.02	0.28 ± 0.11	$(1.19 \pm 0.46)\text{E-7}$
NTB 931008.63	66.56 ± 1.45	$(1.98 \pm 0.28)\text{E+2}$	0.26 ± 0.04	$(3.34 \pm 0.29)\text{E-6}$
NTB 931011.96	11.26 ± 3.24	50.18 ± 18.55	0.20 ± 0.11	$(2.00 \pm 1.27)\text{E-7}$
NTB 931014.08	...	4.10 ± 2.05	0.36 ± 0.14	$(1.24 \pm 0.52)\text{E-7}$
NTB 931017.22	9.22 ± 5.22	41.98 ± 23.57	0.16 ± 0.06	$(2.72 \pm 1.82)\text{E-7}$
NTB 931020.10	21.50 ± 3.24	73.73 ± 2.29	0.14 ± 0.05	$(4.52 \pm 1.52)\text{E-7}$
NTB 931025.93	20.48 ± 9.22	49.15 ± 15.66	0.21 ± 0.05	$(5.15 \pm 2.55)\text{E-7}$
NTB 931031.23	...	1.02 ± 0.00	0.40 ± 0.11	$(8.95 \pm 2.43)\text{E-8}$
NTB 931106.48	31.74 ± 2.29	90.11 ± 1.45	0.22 ± 0.04	$(1.41 \pm 0.21)\text{E-6}$
NTB 931106.90	...	11.26 ± 4.10	0.32 ± 0.06	$(2.66 \pm 0.50)\text{E-7}$
NTB 931107.31	30.72 ± 3.24	55.30 ± 9.27	0.41 ± 0.11	$(1.57 \pm 0.40)\text{E-6}$
NTB 931111.71	58.37 ± 3.07	$(1.86 \pm 0.01)\text{E+2}$	0.77 ± 0.04	$(7.24 \pm 0.59)\text{E-6}$
NTB 931113.04	12.29 ± 1.02	52.22 ± 16.67	0.21 ± 0.05	$(4.15 \pm 0.93)\text{E-7}$
NTB 931115.77	14.34 ± 1.45	26.62 ± 2.29	0.32 ± 0.06	$(3.15 \pm 0.76)\text{E-7}$
NTB 931125.86	5.12 ± 1.02	14.34 ± 1.45	0.83 ± 0.05	$(1.27 \pm 0.27)\text{E-6}$
NTB 931206.45	11.26 ± 1.02	29.70 ± 8.44	0.26 ± 0.05	$(5.43 \pm 1.11)\text{E-7}$
NTB 931209.89	34.82 ± 1.02	90.11 ± 4.58	0.27 ± 0.06	$(1.44 \pm 0.21)\text{E-6}$
NTB 931215.12	3.07 ± 2.05	13.31 ± 11.31	0.28 ± 0.07	$(2.25 \pm 1.61)\text{E-7}$
NTB 931220.16	4.10 ± 1.45	11.26 ± 4.10	0.49 ± 0.11	$(6.84 \pm 2.81)\text{E-7}$
NTB 931220.73	8.19 ± 0.00	33.79 ± 4.58	0.56 ± 0.05	$(9.78 \pm 0.89)\text{E-7}$
NTB 931222.11	18.43 ± 3.24	58.37 ± 12.83	0.18 ± 0.06	$(6.86 \pm 1.93)\text{E-7}$
NTB 931222.82	...	2.05 ± 1.02	1.75 ± 0.24	$(4.40 \pm 0.65)\text{E-7}$
NTB 931223.07	...	3.07 ± 1.02	0.26 ± 0.19	$(9.55 \pm 7.28)\text{E-8}$

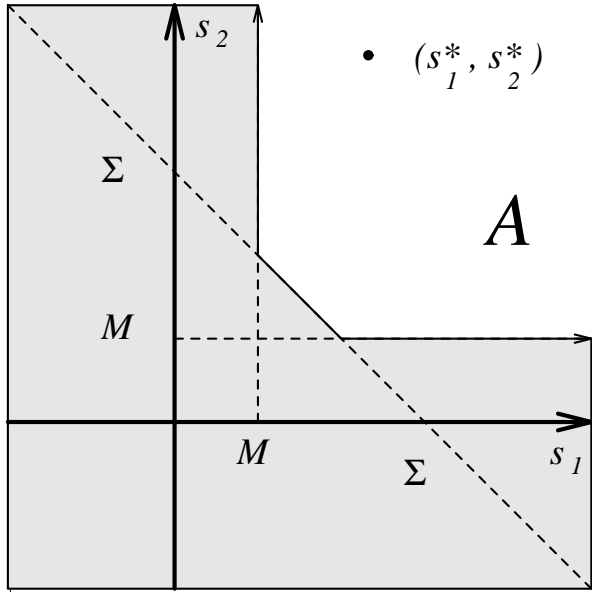


Fig. 1.—

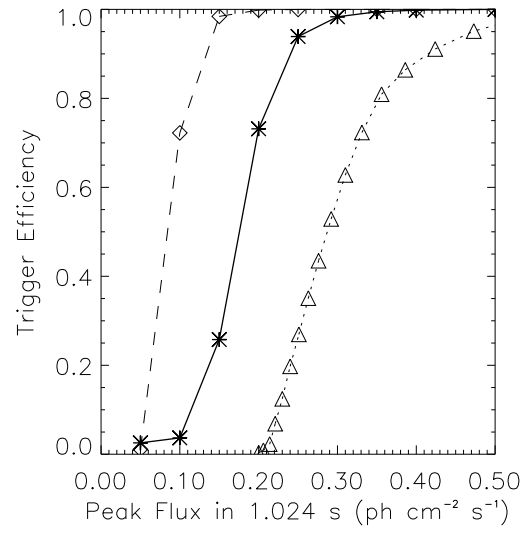


Fig. 3.—

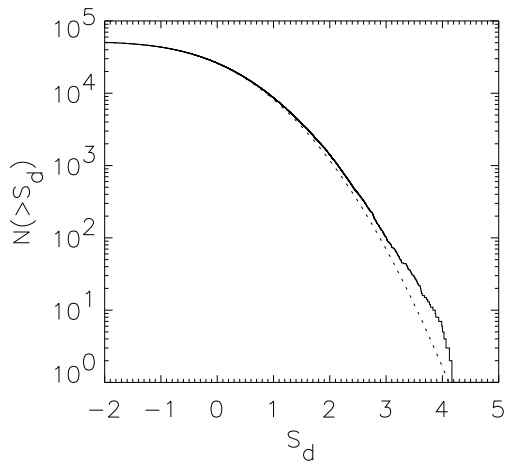


Fig. 2.—

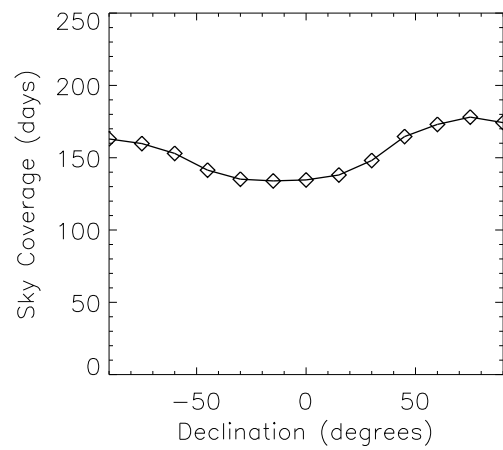


Fig. 4.—

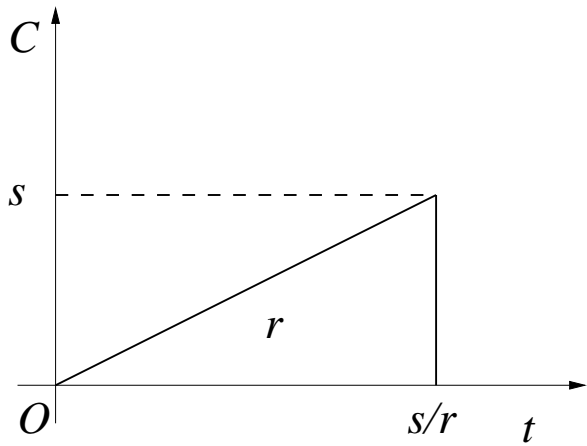


Fig. 5.—

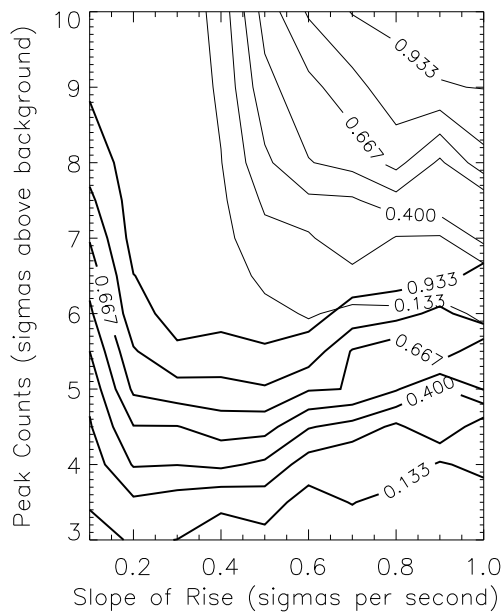


Fig. 6.—

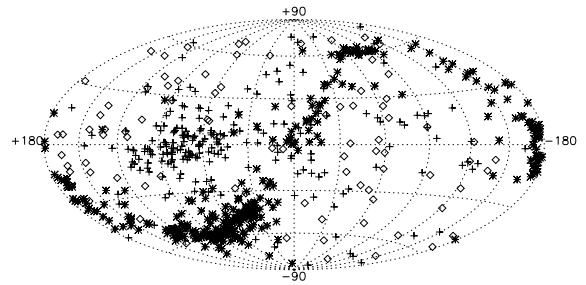


Fig. 7.—

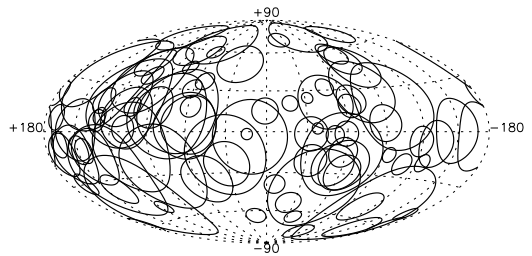


Fig. 8.—

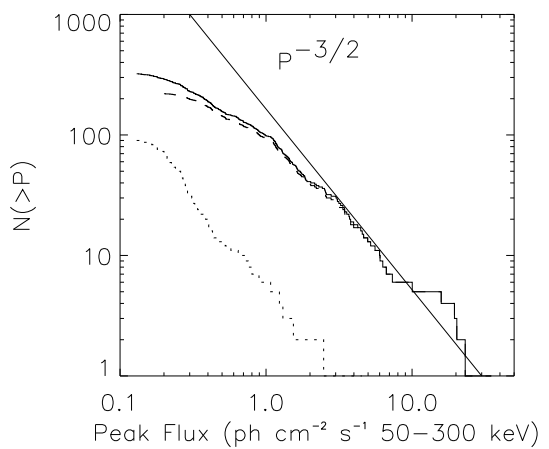


Fig. 9.—

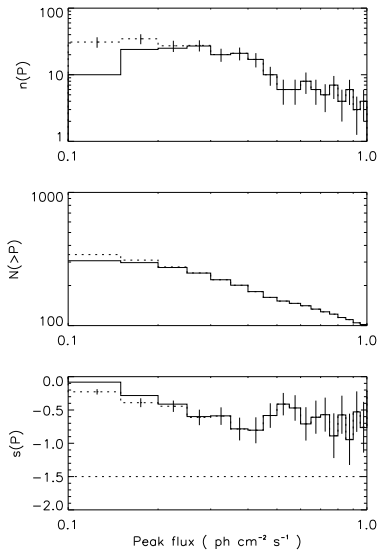


Fig. 10.—

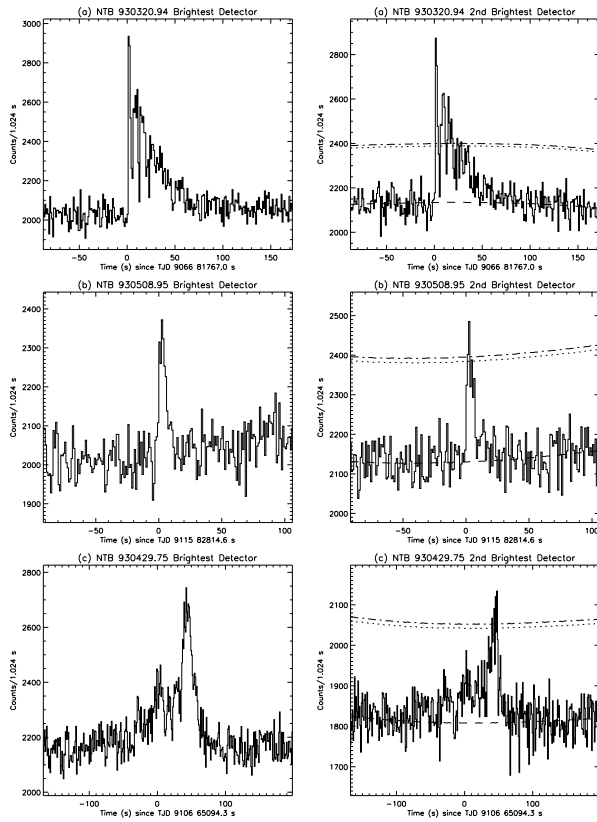


Fig. 11.— page 1

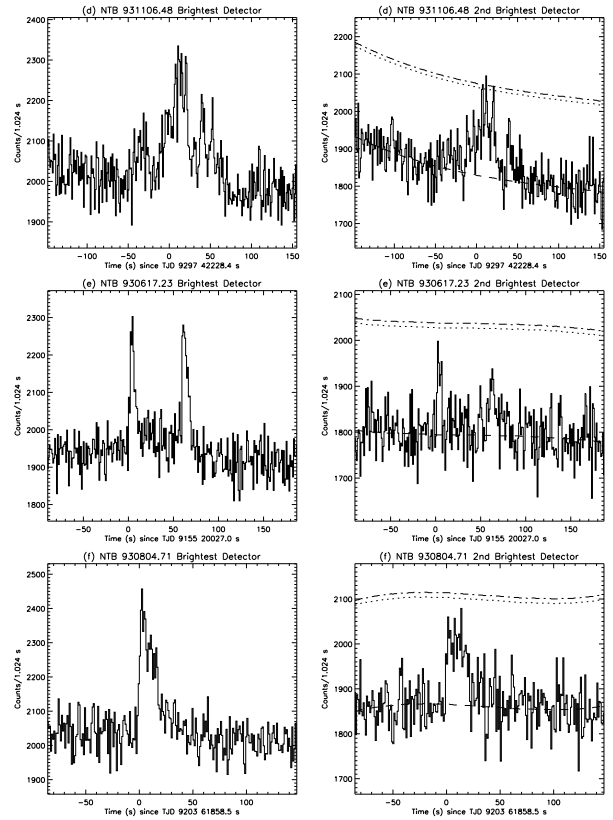


Fig. 11.— page 2

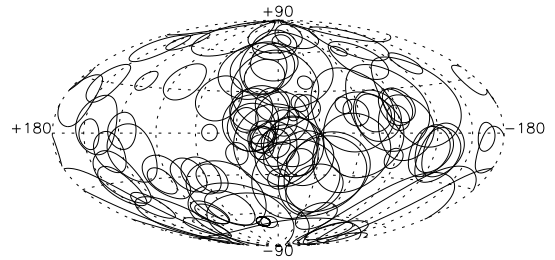


Fig. 12.—